Annals of Nuclear Energy 110 (2017) 475–485

Contents lists available at ScienceDirect

Annals of Nuclear Energy

journal homepage: www.elsevier.com/locate/anucene

High-fidelity multi-physics coupling for determination of hydride distribution in Zr-4 cladding

Ian Davis [a], Olivier Courty [a], Maria Avramova [b,*], Arthur Motta [a]

[a] The Pennsylvania State University, Department of Mechanical and Nuclear Engineering, 138A Reber Building, University Park, PA 16802, United States
[b] North Carolina State University, Department of Nuclear Engineering, Campus Box 7909, Raleigh, NC 27695, United States

ARTICLE INFO

Article history:
Received 26 December 2016
Received in revised form 21 June 2017
Accepted 26 June 2017
Available online 15 July 2017

ABSTRACT

Hydride production in Zircaloy cladding continues to be one of the main limiting factors for extending the life of nuclear fuel rods in the core. The production of hydrides in the cladding comes as a direct result of corrosion with water during normal operation. Furthermore, the distribution of hydrogen in the cladding depends strongly on the temperature and temperature gradients inside the cladding. In order to accurately predict these temperature gradients, a high-fidelity multi-physics coupling is needed. The Department of Energy (DOE) recognized this need and sponsored a project at the Pennsylvania State University (PSU) in cooperation with North Carolina State University (NCSU) under the Nuclear Energy University Programs (NEUP). The overreaching goal of this project is to couple thermal-hydraulics, neutronics, and fuel performance codes together to predict the distribution of hydrogen and hydrides in the cladding as a function of time and space. This goal is attained through a two-step approach. The first step combines accurate high-fidelity thermal-hydraulic models for heat transfer, reactor physics models for neutron flux, and thermal-mechanics models for fuel performance calculations to acquire detailed temperature and stress distributions in the fuel rod. The second step develops a semi-analytical model and experimentally tests the temperature and/or stress dependent hydrogen pick-up, diffusion, and precipitation in the cladding. This paper aims to show the capabilities of the high-fidelity coupling, their effect on the power and temperature predictions, and subsequent effect on the distribution of hydrogen in the cladding, specifically in the inter-pellet gap region.

1. Introduction

Nuclear reactors are complex systems used for generating energy from nuclear fission. The fission process results in the production of fission fragments that might be radioactive or present a risk to the public health. Therefore, these fragments should be retained within the fuel. The fuel cladding serves as the first barrier against the release of such fission products to the environment outside the nuclear power plant. The fuel cladding should preserve its integrity during the whole lifetime of the fuel inside the reactor and during its storage as a spent fuel (INSAG, 1996).

Zirconium alloys are extensively used as a fuel cladding for Light Water Reactors (LWRs). Zirconium based alloys are preferred because of their low thermal neutron absorption cross sections, relatively high melting temperature, and good corrosion and fracture resistance. Zircaloy-2 (Zr–1.5Sn–0.12Fe–0.1Cr-0.05Ni in wt%) is used as a cladding material for Boiling Water Reactors (BWRs) while Zircaloy-4 (Zr–1.5Sn–0.2Fe–0.1Cr–0.007Ni in wt%) is used as a cladding for Pressurized Water Reactors (PWRs) (Sawatzky and Ells, 2000).

One of the factors that might affect the integrity of the fuel cladding is the formation of hydride precipitates. The high velocity of the water used as a coolant for LWRs is a highly corrosive environment to the zirconium cladding. This corrosive action involves the oxidation of the cladding accompanied by the release of hydrogen. A fraction of this released hydrogen can be picked-up by the cladding to form a solid solution. The hydrogen tends to diffuse from higher concentrations to lower concentrations regions (Fick's law), and from higher temperatures to lower temperatures regions (Soret effect). Depending on the concentration and temperature, the hydrogen may form localized hydride precipitates that might embrittle the cladding locally. This makes the cladding vulnerable to cracking and its integrity might be compromised. At a specific axial height, radial location, and azimuthal angle the local hydride concentration might be very high forming a weak point in the cladding.

It is important to model the diffusion of hydrogen and the local formation of hydrides to be able to quantify their effects on the

* Corresponding author.
E-mail addresses: ijd5004@gmail.com (I. Davis), acourty1@gmail.com (O. Courty), mnavramo@ncsu.edu (M. Avramova), atmnuc1@psu.edu (A. Motta).

http://dx.doi.org/10.1016/j.anucene.2017.06.049
0306-4549/

cladding. A model of this process has been implemented in BISON fuel performance code as described in this paper in order to quantify the local hydrogen effect. The input and boundary conditions (outer fuel rod cladding temperature distribution) to this model are provided by performing high-fidelity multi-physics calculations, based on coupling of thermal-hydraulics, neutronics, and fuel performance codes.

1.1. Heterogeneous distribution of Hydrogen/Hydrides in cladding

Hydrogen enters the cladding through a corrosion reaction with water, given by Eq. (1):

$$Zr + 2H_2O \rightarrow ZrO_2 + 2H_2 \quad (1)$$

This corrosion reaction forms a zirconium oxide layer on the waterside of the fuel rod, and diminishes the heat transfer properties of the alloy. Though the corrosion is a continuous process, only 10–20% of the hydrogen released by the reaction migrates into the cladding; the majority is carried away in the coolant. Therefore, the process is relatively slow, and fuel rods generally last about three cycles (3–5 years) before they must be removed from the core. Current Unite States (US) Nuclear Regulatory Commission (NRC) regulations place a 62 GWd/MTU burnup limitation on fuel rods, which is driven by both the lack of sufficient reactivity left in the pellets and also the level of corrosion in the cladding.

1.2. Hydrogen diffusion dependencies

Once inside the zirconium alloy, hydrogen distributes in the cladding of nuclear fuel rods in a highly heterogeneous fashion. Two phenomena are attributed to the diffusion of hydrogen in cladding: Fick's Law and the Soret Effect. Fick's Law dictates that hydrogen in solid solution diffuses by a concentration gradient, moving from areas of higher concentration to lower concentration. The Soret Effect describes the diffusion of hydrogen atoms by a temperature gradient, migrating from areas of higher temperature to lower temperature. From an article in the Journal of Nuclear Materials, Sawatzky developed a semi-analytical equation to describe the diffusion of hydrogen in solid solution (Sawatzky, 1960). In the presence of concentration and temperature gradients, the diffusion of hydrogen is given by Eq. (2):

$$J = -\frac{DN}{RT}\left(RT\frac{d(\ln(N))}{dx} + \frac{Q^*}{T}\frac{dT}{dx}\right) \quad (2)$$

where J is the diffusion flux, D is the diffusion constant of hydrogen in zirconium, N is the concentration of hydrogen in solid solution, R is the gas constant, T is the temperature, and Q^* is the heat of transport (empirical value according to the Soret Effect) (Sawatzky, 1960).

As more hydrogen diffuses into the cladding, a concentration gradient causes hydrogen to disseminate inward from the outer edge of the cladding. Recall that a temperature gradient also affects the hydrogen diffusion. Moreover, hydrogen tends to diffuse in the opposite direction of positive temperature gradients (i.e. towards colder regions). Temperatures and temperature gradients can vary in all three dimensions (r,θ,z) independent of each other. In the radial (r) direction, the fuel pellet inside the cladding is a heat source, while the water outside the cladding acts as a heat sink. The temperature drops roughly 30–40 °C across the width of the cladding (Geelhood et al., 2011). In the azimuthal (θ) direction, geometric heterogeneity can play a role in altering the temperature gradients. For example, a fuel rod next to a guide tube encounters colder moderator temperatures on that side adjacent to the guide tube compared to the other three sides, which are next to other fuel pins. In addition, fuel rods located on the outer edges of the core may encounter temperature gradients from the core interior to the reflector region outside the fuel assemblies. In the axial (z) direction, coolant enters the core at about 287 °C and exits at around 320 °C (Geelhood et al., 2011). The axial temperature gradient in the coolant directly affects the axial temperature gradient in the cladding. In addition, the energy deposition from the fuel pellets is not uniform in the axial direction. As a simple approximation, the axial power distribution follows the cosine function with the peak energy deposition occurring halfway along the active fuel length. This also has a direct effect on the temperature profiles inside the cladding material. On a much smaller scale, current fuel pellet manufacturing practices often include dishes and chamfers in the pellet geometry to provide extra space for fission gas release, thermal expansion, and swelling. Refer to Fig. 1, which comes from an article in the Journal of Nuclear Materials authored by the Idaho National Laboratory (INL), and shows a shape of (real) fuel pellets including inter-pellet gaps in the axial (z) direction along with the Finite-Element Mesh used in the fuel performance code BISON to model fuel pellets (Williamson et al., 2012b). Temperature gradients form in the inter-pellet gaps solely because there is less fuel material in this region of the rod. Less fuel material means less fission, which means less energy deposition in the cladding. Considering both the variability in the concentration and temperature gradients, it is clear to notice the complex nature of hydrogen diffusion in cladding.

Over time as more hydrogen ingresses into the cladding, the concentration of hydrogen in solid solution approaches the Terminal Solid Solubility for precipitation (TSSp) limit (McMinn et al., 2000; Kearns, 1967). Above this limit, hydrogen in solid solution precipitates into hydrides. It is important to note that the Terminal Solid Solubility (TSS) follows an Arrhenius law, and is different for hydride precipitation versus dissolution. Specifically, for given hydrogen concentration (wt.ppm) the temperature required to precipitate is lower than the temperature required to dissolve hydrides, creating a hysteresis effect.

Once hydrides begin to precipitate in the cladding, the material properties start to degrade. Kimberly Colas notes in her dissertation that hydrides are notably brittle in tension, with a fracture toughness less than 2 MPa at room temperature and less than

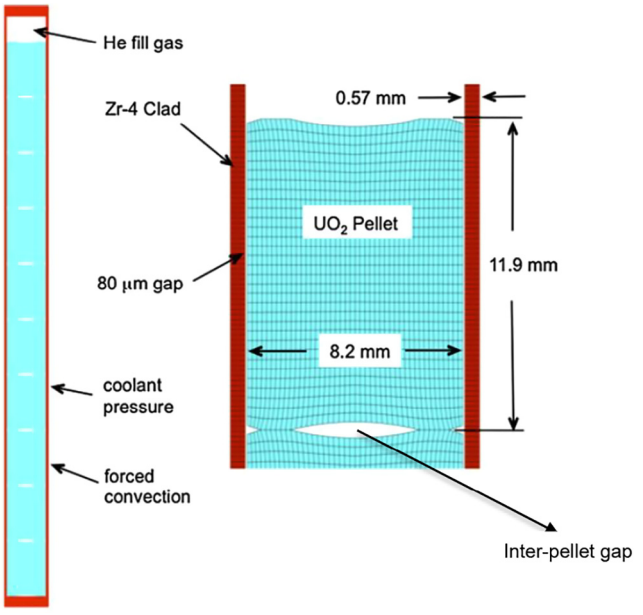

Fig. 1. Example FEM Mesh for a 10 Pellet Model in BISON (Williamson et al., 2012b).

4 MPa at 300 °C (Colas, 2012). Colas also references a study done by Xu et al., which compared some material properties of zirconium hydrides ($ZrH_{1.83}$) to pure zirconium (Zr), and presents the information shown in Table 1 (Xu and Shi, 2004).

While these mechanical properties were measured well below normal operating temperatures, the effect of containing a far more brittle species in zirconium alloys is clear, especially if the amount is significant.

2. Description of computer codes

2.1. The subchannel thermal-hydraulic code CTF

CTF (an improved version of COBRA-TF) is a two-fluid, three-field subchannel analysis code capable of modeling any vertical one-, two-, or three-dimensional component in the reactor vessel (Avramova, 2016). CTF is a modernized and further improved version of COBRA-TF that is maintained and further developed at North Carolina State University (NCSU). In CTF the fluid field is divided into a continuous liquid field, and entrained liquid droplet field, and a vapor field. Like many thermal-hydraulic analysis codes, the equations of the flow field in CTF are solved using a staggered difference scheme in which the velocities are obtained at the mesh faces and state variables are obtained at the cell center. CTF allows heat transfer surfaces and solid structures that interact significantly with the fluid to be modeled as rods and unheated conductors. CTF allows many parameters to be specified by the user or determined using benchmarked empirical correlations. In the last decade, CTF has been improved (including translation to FORTRAN 95), further developed and extensively validated for both Pressurized Water Reactor (PWR), and Boiling Water Reactor (BWR) applications. Attention has been given to improving code error checking and the input deck has been converted from fixed to free format. Then Krylov solver based numerical techniques have been implemented to enhance computational efficiency. Improvements have been made to the turbulent mixing and direct heating models, and code quality assurance testing has been performed using an extensive validation and verification matrix. Finally, to improve code usability and enable easier future modifications and improvements, code documentation (including theory, programming, and user manuals) has been prepared. Nowadays it is one of the state-of-the-art codes for Light Water Reactor (LWR) thermal-hydraulic analyses. Concerning this research, the CTF applicability to PWR operation conditions in terms of temperature and pressure ranges has been previously established and validated. The utilized mesh size in radial plane is on sub-channel scale – see Fig. 3a. Four sub-channels surround each fuel rod.

2.2. The neutronics code DeCART

DeCART (Deterministic Core Analysis based on Ray Tracing) is a Method Of Characteristics (MOC) neutronics code (Kochunas et al., 2009; Hursin et al., 2008). DeCART was originally developed by KAERI as part of a United States – Republic of Korea (US-ROK) collaborative National Energy Research Institute (I-NERI) project between KAERI, ANL, and Purdue University. US Department Of Energy (DOE), Electric Power Research Institute (EPRI), and Advanced Fuel Cycle Initiative (AFCI) have supported further development in the U.S. The University of Michigan is also a major supporter of DeCART and its development. Regarding the actual models in the code, DeCART is capable of modeling whole core simulations while calculating direct sub-pin level heterogeneous fluxes at power generating conditions of a PWR and BWR. The depletion and transient simulations are available. Input parameters include geometry, material composition, thermal operating conditions, and program execution control parameters. The DeCART mesh in radial plane is more detailed than the CTF mesh and sub-divides the pin (fuel rod) plus surrounding moderator/coolant region in cells formed by rings and sectors as shown in Fig. 3b. In axial direction, the CTF and DeCART mesh coincides and consists of axial nodes. Approximation known as "flat source regions" is applied to radial cells and axial nodes and "step function" is used subsequently for the discretization of the output power profile to be used as input to CTF and BISON.

Table 1
Mechanical Properties of Zr and $ZrH_{1.83}$ at Room Temperature.

Material	Modulus (Gpa)	Hardness (Gpa)	K_{IC} (MPa/m)
Zr	80.9	4.9	~40
$ZrH_{1.83}$	~66	3.3	0.74

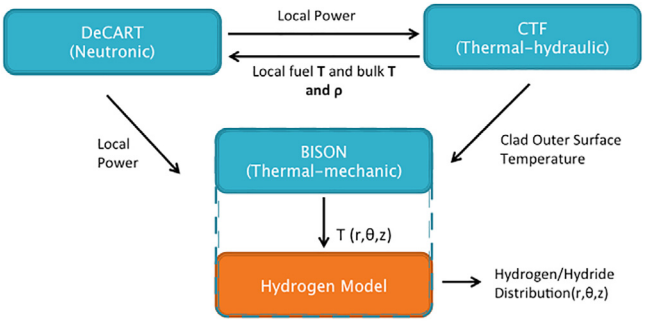

Fig. 2. External Coupling Diagram Between CTF, DeCART, and BISON.

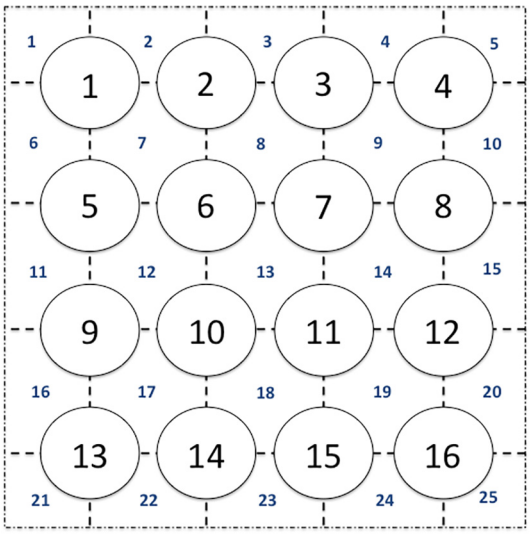

Fig. 3a. CTF 4 × 4 PWR Sub-Assembly Layout.

2.3. The fuel performance code BISON

BISON is a nuclear fuel performance analysis tool that is currently under development at the INL (Williamson et al., 2012a,b). BISON was built using MOOSE (Multi-physics Object Oriented Simulation Environment) (Derek Gaston, 2012). MOOSE is a multi-physics application framework designed to significantly reduce the expense and time required to develop new applications. BISON is a finite element code that can model a single fuel pin, individual fuel pellet(s), or any single geometry element desired in two or three dimensions. The Two-Dimensional (2D) r-z mesh used in this

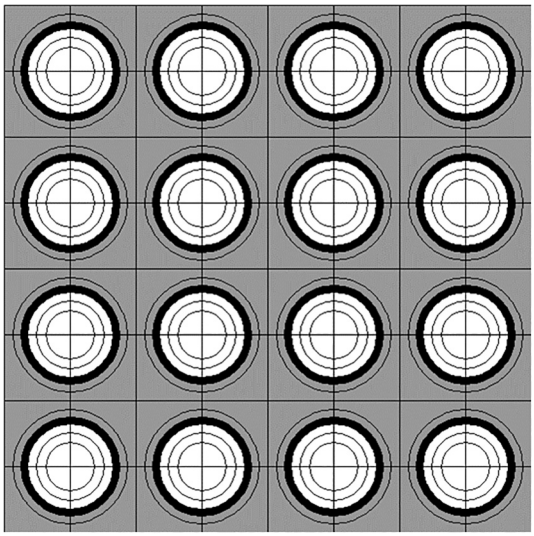

Fig. 3b. DeCART 4 × 4 Sub-Assembly Diagram.

research is shown in Fig. 3c. Input parameters include the mesh file for geometry, operating conditions, thermal and mechanical boundary conditions, etc. BISON stores all output information to the mesh file, which can be analyzed in a visualization tool, such as Paraview (Laboratory, 2013).

3. Code coupling

Code coupling between the neutronics, thermal-hydraulics, and fuel performance allows for modeling the feedback effects in the reactor core, and combining of each of the code's strengths. Neutronics is particularly focused on cross-section generation and sub-sequent fission energy deposition calculations; thermal-hydraulics performs the heat transfer and fluid mechanics calculations within the coolant; and fuel performance determines the thermal and mechanical behavior of the fuel and clad material in the fuel rod. Furthermore, using the code coupling allows the user to develop a better and more realistic all-around model of the fuel rod.

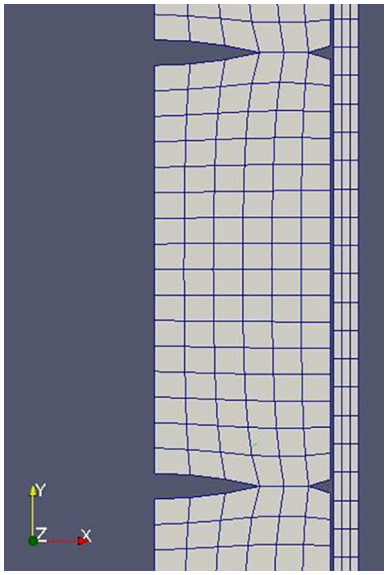

Fig. 3c. 2D r-z Mesh used in BISON.

Exchange parameters are those variables, which are passed from one code to another. To improve upon the thermal-hydraulics calculations in CTF, the code needs feedback from the neutronics code for power distribution in the fuel rods. Specifically, the axial power distribution (relative local power with respect to the axial direction), in-pellet radial power distribution (relative local power with respect to the radial location inside the fuel pellet), and the radial power factor (the total relative power of one rod compared to the average power of the array) are provided from DeCART to CTF.

CTF and DeCART are externally coupled together with bi-directional (two-way) feedback. The coupling between DeCART and BISON is one-way with only feedback from DeCART to BISON. The coupling between CTF and BISON is one-way with only feedback from CTF to BISON. Fig. 2 below shows the general coupling scheme. The notation "bulk T and ρ" means coolant/moderator temperature and density.

The output from BISON represents the connection from the two sides of this project. With a cladding temperature distribution as a function of space and time known, this information is passed to the Hydrogen Model, which is incorporated directly into BISON. Results from the Hydrogen Model simulations are hydrogen/hydride distributions in the cladding as a function of space and time. Simulation can be adapted to two-dimensional or three-dimensional models. The work presented in this paper highlights the hydrogen distributions for small-scale two-dimensional models in the radial and axial directions.

4. Hydrogen model

A model describing the behavior of hydrogen in Zircaloy-4 was derived from the equation given in Section 1.2. The global model is described in Section 4.1. Then, the model was implemented into the fuel performance code BISON, as explained in Section 4.2. Details of this implementation are given in the Olivier Courty's thesis (Courty, 2013).

4.1. Balance equations Description

From the precipitation, dissolution, and diffusion models, the balance equation for hydrogen in solid solution and hydride concentration can be deduced. The variation of hydrogen in solid solution per unit of time is given by the sum of the net flux, the hydrogen created by the dissolution of hydride minus the hydrogen transformed into hydride due to precipitation. Based on the Sawatzky diffusion model given by Eq. (2), the diffusion flux is equal to:

$$J = -D\nabla C_{ss} - \frac{DC_{ss}Q^*}{RT^2}\nabla T \tag{3}$$

where J_D is the diffusion flux, C_{ss} is the concentration of hydrogen in solid solution, R is the gas constant, T is the temperature in Kelvin, and Q^* is the heat of transport.

Hydride precipitation occurs when the C_{ss} surpasses the TSSp. Hydride dissolution occurs when the C_{ss} becomes lower than the Terminal Solid Solubility of dissolution (TSSd). The TSSp and TSSd values measured by McMinn (McMinn et al., 2000) have been used for the current work:

$$\begin{bmatrix} TSSd(wt.ppm) = 106446.7\exp\left(-\frac{4328.67}{T(K)}\right) \\ TSSp(wt.ppm) = 138746.0\exp\left(-\frac{4145.72}{T(K)}\right) \end{bmatrix} \tag{4}$$

According to Marino's Equation (Laboratory, 2013), the rate of precipitation (in wt.ppm/s) is given by:

$$R_{precipitation} = -\alpha^2(C_{ss} - TSSp) \quad (5)$$

where α^2 is the precipitation rate constant, and TSSp is the Terminal Solid Solubility limit of precipitation.

The dissolution is assumed instantaneous by most authors and is assumed here. In order to simplify future calculations, a linear law for the dissolution is assumed, with a characteristic time very small compared to the precipitation characteristic time:

$$R_{dissolution} = \beta^2(C_{ss} - TSSp) \quad (6)$$

Note: $\beta \gg \alpha, \beta \gg \frac{l^2}{D}$, β is the dissolution rate constant, D is the diffusion coefficient, and l is the length.

The diffusion coefficient is calculated using Kearns' correlation (Kearns, 1972):

$$D = A_{diff} exp\left(-\frac{Q_{Diff}}{RT}\right) \quad (7)$$

The coefficients have been measured by Kearns:

$$A_{diff} = 7.90 * 10^7 \ m^2/s;$$

$$Q_{diff} = 4.49 * 10^4 \ J/mol$$

Four different cases have to be taken into account for the writing of the balance equations. In the first case, the concentration of hydrogen in solid solution is greater than the TSSp. Then, precipitation occurs according to the laws described above:

- Precipitation:

$$if \ C > TSSp, \left\{ \begin{array}{c} \frac{dC_{ss}}{dt} = -\nabla J - \alpha^2(C_{ss} - TSSp) \\ \frac{dC_p}{dt} = \alpha^2(C_{ss} - TSSp) \end{array} \right\} \quad (8)$$

In the second case, the concentration in solid solution is between the TSSp and the TSSd. This is the "hysteresis" area, where neither diffusion nor precipitation occurs:

- Hysteresis:

$$if \ \ TSSp \geq C > TSSd, \left\{ \begin{array}{c} \frac{dC_{ss}}{dt} = -\nabla \cdot J \\ \frac{dC_p}{dt} = 0 \end{array} \right\} \quad (9)$$

where Cp is the hydrogen in the precipitated hydrides.

In the third case, the concentration in solid solution is below the TSSd. The hydrogen in the precipitated hydrides (C_p) dissolves so that the C_{ss} matches the TSSd value. This is possible only if there are hydrides ($C_p > 0$):

- Dissolution:

$$if \ TSSd \leq C \ and \ C_p > 0 \ and \ \nabla J > 0, \left\{ \begin{array}{c} \frac{dC_{ss}}{dt} = -\nabla \cdot J + \beta^2(TSSd - C_{ss}) \\ \frac{dC_p}{dt} = -\beta^2(TSSd - C_{ss}) \end{array} \right\} \quad (10)$$

In the fourth and last case, the concentration in solid solution is below the TSSd, but there are no more hydrides to dissolve. In that case, the only change to hydrogen concentration comes from net diffusion flux:

- Diffusion only:

$$if \ \ TSSd \geq C \ \ and \ \ C_p = 0, \left\{ \begin{array}{c} \frac{dC_{ss}}{dt} = -\nabla J \\ \frac{dC_p}{dt} = 0 \end{array} \right\} \quad (11)$$

The model constants have been taken from the literature, and are summarized in Table 2.

4.2. Implementation of the model in BISON

The equations describing the behavior of the hydrogen in Zircaloy-4, introduced in Section 4.1, have been implemented in the fuel performance code BISON. The hydrogen concentration is governed by two balance equations. Since BISON is based on Galerkin Finite Element models, some derivations have to be applied to the equation. They are transformed into what is called their "weak form". The calculation can be found in Olivier Courty's thesis (Courty, 2013).

Usually, the boundary conditions for the hydrogen are expressed in term of flux at the cladding surface. The flux is assumed to be zero for all the surfaces except the cladding/coolant interface. At this interface, the flux can be deduced from the oxidation kinetics values and the pick-up values. These conditions have been used in all of the hydrogen simulations.

BISON is a based on the MOOSE framework, and is a modular code. Once new equations, such as the hydrogen model, are implemented, they are solved internally with all the other equations (i.e. temperature and stress equations). At each time step, the code calculates the value of each parameter, internally coupling the equations. However, the hydrogen model needs very small time steps (<250 s) due to the precipitation kinetics, which is a fast process. On the other hand, the temperature and stress calculation can be made at very large time steps ($\sim 10^6$ s). Calculating the solution for each hydrogen time step in-between depletion time steps is not practical. Moreover, there is no feedback effect implemented from the hydrogen concentration on any of the other parameters. Therefore, the calculation is usually made in two steps. First the temperature and stress values are calculated with large time steps. Then, the hydrogen model is run with small time steps, using interpolated values of the clad temperature from the first calculation. In this manner, the hydrogen model in BISON can run completely separately from the depletion calculations, reducing the overall computational expense of the simulation.

5. Model description

For this test case, a 4×4-pin array comprising only fuel pins was modeled in CTF and DeCART. Figs. 3a and 3b show the fuel pin layout for CTF and DeCART. The fuel rods were modeled after typical PWR specifications; and all general specifications can be seen in Table 3. Some specifications were taken from a study done at Oak Ridge National Laboratory (ORNL), using the Advanced Multi-Physics Nuclear Fuel Performance Code (AMPFuel) (Hamilton et al., 2012). Other specifications were taken from typical PWR inputs built for use in SIMULATE-3, as part of the university version of the Studsvik Scandpower Code System (CMS) for research and education purposes (Studsvik, 2009). Using DeCART's depletion calculations, the 4×4 array was burned up to 40.0 MWd/kgU ($\sim$1036 effective full power days). As a first approximation, no guide tubes or burnable absorbers were included in the 4×4 model; however, such characteristics of PWR's are added once initial testing of the external coupling is completed. In addition, in Fig. 3a the dotted lines separate the 25 subchannels that were modeled around the fuel pins in CTF.

6. Results

6.1. CTF-DeCART coupled calculations

As noted earlier, the parameters of interest for the CTF-DeCART coupling are the axial power distribution and the cladding (clad) outer surface temperature distribution, which are both used as boundary conditions for the BISON code. The axial power distribu-

Table 2
Hydrogen Model Constants.

Phenomenon	Parameter	Value	Unit	Source	Comments
Fick's law	A_{Dff}	7.90×10^{-7}	m^2/s	Kearns (1967)	Longitudinal diffusion
	Q_{Diff}	4.49×10^4	J/mol	Kearns (1967)	Longitudinal diffusion
Soret effect	Q^*	2.51×10^4	J/mol/K	Kammenzind et al. (1996)	Average value
Precipitation	A_P	1.39×10^5	wt. ppm	McMinn et al. (2000)	Unirradiated
	Q_P	3.45×10^4	J/mol	McMinn et al. (2000)	Unirradiated
Dissolution	A_D	1.06×10^5	wt. ppm	McMinn et al. (2000)	Unirradiated
	Q_D	3.60×10^4	J/mol	McMinn et al. (2000)	Unirradiated
Precipitation kinetics	A_α	6.23×10^1	$s^{1/2}$	Kammenzind et al. (1996)	
	Q_α	4.12×10^4	J/mol	Kammenzind et al. (1996)	

Table 3
4×4 PWR Sub-Assembly Specifications.

Type	Value	Units
Reactor	PWR	
Layout	4×4	
Fuel	UO2	
Enrichment	3.45%	
Fuel density	10.4	g/cm^3
% of theoretical density (10.96 g/cc)	95%	
Burnable poison	None	
Clad	Zircaloy-4	
Clad density	6.55	g/cm^3
Coolant	H_2O	
Fill gas	Helium	
Fill gas density	0.0002	g/cm^3
Fuel pellet radius	0.4095	cm
Clad inner radius	0.418	cm
Clad outer radius	0.475	cm
Clad thickness	570	microns
Pin pitch	1.26	cm
Active fuel height	365.76	cm
Top reflector height	35.512	cm
Bottom reflector height	35.512	cm
Array power	1.0808	MW
Average linear heat rate	18.5	kW/m
Core pressure	15.5	Mpa
Mass flow rate	4.86	kg/s
Beginning of Cycle (BOC) boron loading	1000	ppm
Inlet temperature	287	°C

tion is combined with the linear heat rate of the rod and a nominal energy per fission ratio to determine the energy deposition. The power and temperature results are shown below. Fig. 4 depicts the axial power distribution for Rod 7 in the sub-assembly as a function of burnup. Fig. 5 shows the clad outer surface temperature as a function of axial position and also burnup.

Regarding the BOL time step from Fig. 4, for the converged solution the axial power distribution is slightly bottom-peaked; peak axial power occurs at ~ 40% of the active fuel height. As depletion progresses, the fuel becomes more burned near the center of the rod compared to the ends of the rod. A greater level of burnup near the center of the rod suppresses the relative power in that region. In addition, more fission products build up near the axial center of the rod, adding to the effect of the power suppression. Observe the axial power shape at EOL 40.0 MWd/kgU; the axial power shape evolves from slightly bottom-peaked to flat and finally to top-peaked. The evolution of axial power shape can be directly attributed to the 'axial offset anomaly'. The US NRC released a report prepared by ORNL in 2002, which discusses the effects of axial offset (Wagner et al., 2003). Specifically, Wagner attributes the axial offset seen in commercial PWRs to the difference in moderator density along the active fuel length; higher density moderator near the core inlet results in higher reactivity in that region, which increases the burnup at the bottom of the core faster than the top. At the same time, Wagner also notes that there are other factors that help to cause axial offset (i.e. control rod insertion, non-uniform operating history, etc.). Nevertheless, the effects of axial offset described in Wagner's report are clearly seen in the evolution of the axial power shape in Fig. 4. Referring to Fig. 5 the clad outer surface temperature profiles follow the same pattern as the power. At BOL the peak location of the clad outer surface temperature occurs at a lower elevation than at EOL. Again, this is an expected result of the axial power shape flattening out and eventually becoming top-peaked.

It is also important to observe the effect that the coupled calculations have on the main parameter of interest for the hydrogen model, clad temperature, compared to calculations without the coupling. Therefore, the figures below show comparisons between

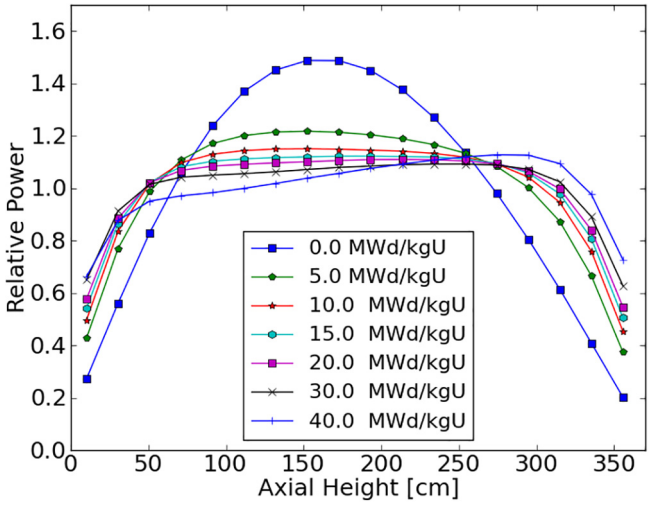

Fig. 4. Rod 7 Converged Axial Power Distributions.

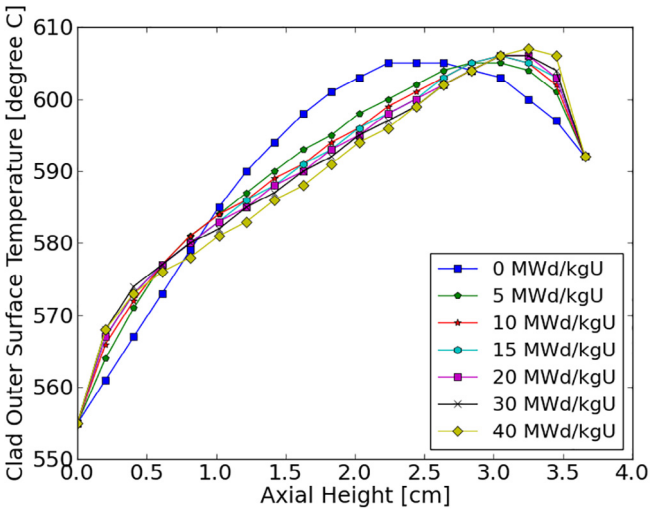

Fig. 5. Rod 7 Clad Outer Surface Temperature Distributions.

BISON simulation with coupled boundary conditions, and a simulation with power distributions from a standalone DeCART run and the use of BISON's internal thermal-hydraulics model. To calculate the temperature of the coolant and the heat transfer coefficient internally, BISON uses the Dittus-Boelter correlation. Another thing to consider is that BISON does not contain any models for neutronics calculations. This information must be provided in the form of fission rates or a combination of linear heat rates, power distributions, and an energy per fission conversion factor. As a result, the choice was made to perform a standalone DeCART calculation to calculate the necessary neutronics information. Power distribution data for the BOL, at one year, and at two years was taken from DeCART and provided to BISON for the standalone calculation without coupled boundary conditions. Fig. 6 shows a comparison of the axial power distribution for the coupled and standalone DeCART calculations at BOL. Fig. 7 shows the same comparison, at one year while Fig. 8 shows the comparison at two years.

Note that the data in Fig. 6 is shown using step functions. DeCART uses what are called 'flat source regions' to discretize the power distribution in the axial direction. This is done because power relates directly to neutron flux, which is always associated with some area or volume. Thus, the power distribution cannot be described at a single point. Rather, the power is averaged over some spatial discretization, and in this case, that discretization is a 'flat source region.' As a result, the correct way to implement the power distribution as a boundary condition in BISON is through a step function.

With the boundary conditions now known, the two BISON simulations were run. Note that the hydrogen model was not included in these simulations. Results below show the cladding temperature calculated by BISON. Figs. 9 and 10 below shows a comparison for the clad outer surface temperature in BISON for simulations with and without the use of coupled boundary conditions. The data was extracted at one day and one year into the simulation, respectively.

Referring to Fig. 9, the gray data points represent the clad outer surface temperature distribution that comes from the coupled boundary conditions. Furthermore, these data points are directly taken from CTF and supplied to BISON. The average discrete temperatures provided by CTF had to be converted to a continuous domain on the cladding surface in order to be able to use them in the BISON model. To be able to do this, a parsed function was created and used to linearly interpolate the temperatures at the outer surface of the fuel between the specific CTF average temperatures The black data points represent the clad outer surface temperatures calculated using BISON's internal Thermal-Hydraulics (T-H) model. Some important observations to note are found near the bottom and top of the fuel rod. At the very bottom of the rod, the BISON simulation without coupled boundary conditions shows an almost instantaneous jump in clad temperature from the inlet to the beginning of the heated section of the fuel rod. Conversely, the coupled boundary conditions result in a more constant increase of clad temperature without much change in slope. Near the top of the fuel rod, the clad outer surface temperature calculated without coupled boundary conditions shows several changes in slope. These sudden changes in slope are unexpected, as the linear heat rate is constant over the rod and is only affected by the power profile shown in Fig. 6. Moreover, the power profile from the standalone DeCART calculation at one day does not warrant the type of temperature shift that is shown near the top of the rod in Fig. 9. Finally, the simulation using coupled boundary conditions do not show this behavior; rather, there is a smooth downward trend in clad temperature near the top of the rod, as expected.

The clad outer surface temperature profiles shown in Fig. 10 generally follow the same shape. Similar to the temperature profiles at one day, the most significant differences in calculations can be observed near the bottom and top of the fuel rod. Again,

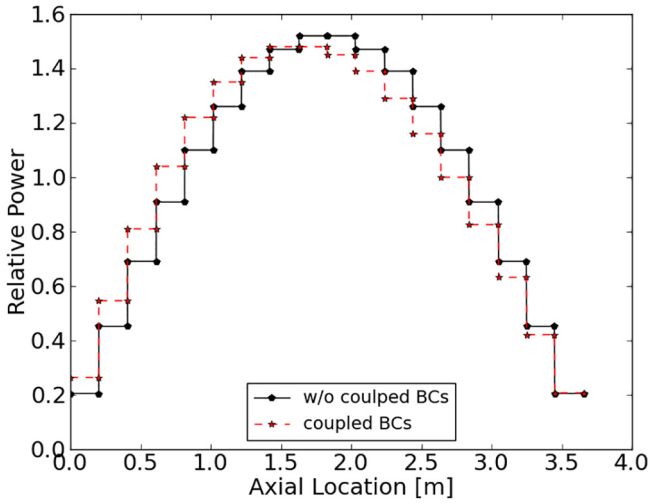

Fig. 6. Rod 7 Axial Power Distribution at BOL.

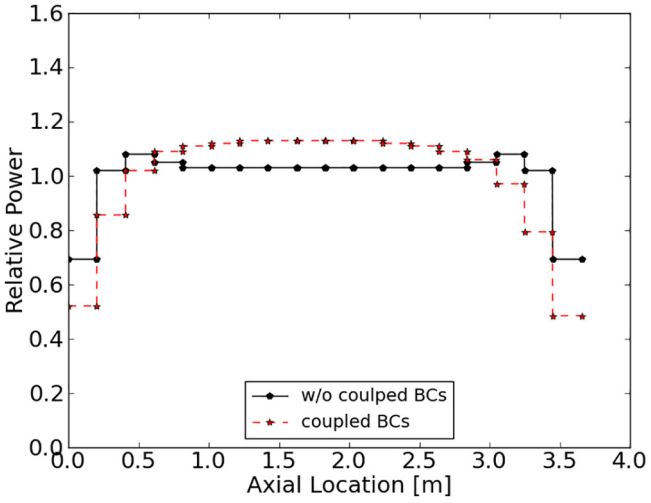

Fig. 7. Rod 7 Axial Power Distribution at One Year.

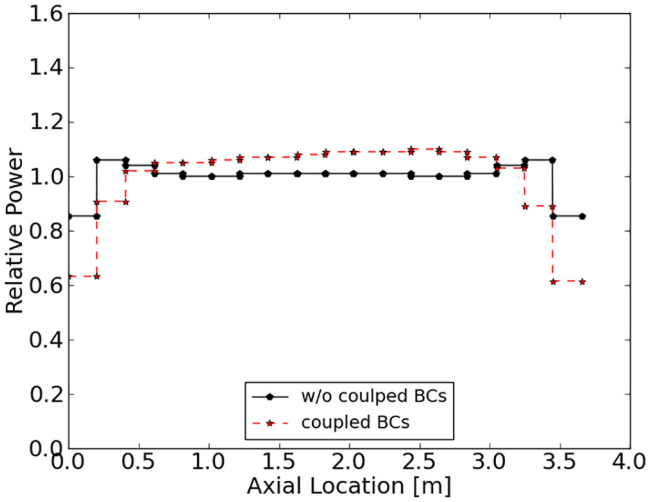

Fig. 8. Rod 7 Axial Power Distribution at Two Years.

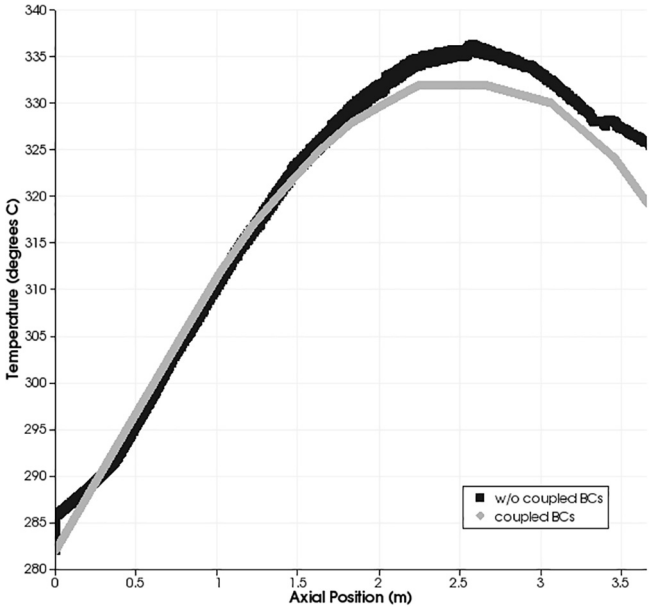

Fig. 9. Clad Outer Surface Temperature at One Day.

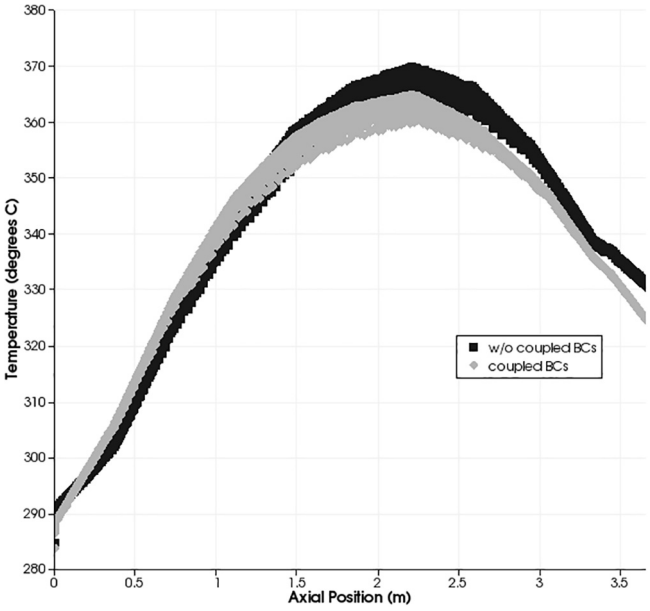

Fig. 11. Clad Inner Surface Temperature at One Day.

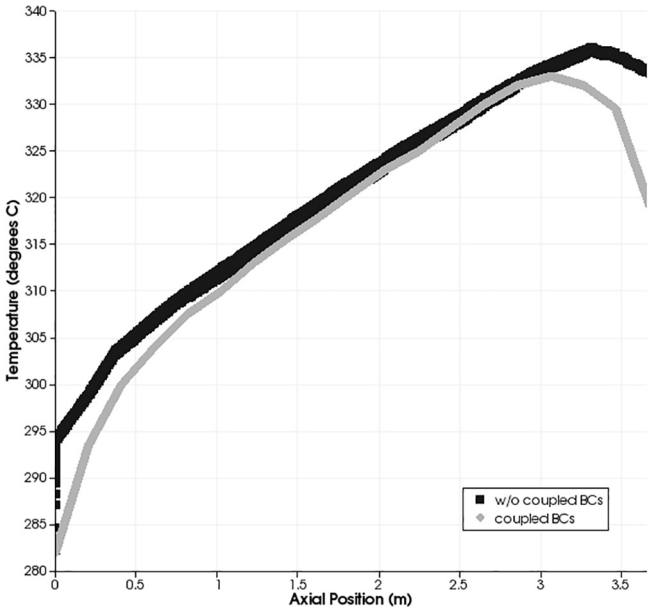

Fig. 10. Clad Outer Surface Temperature at One Year.

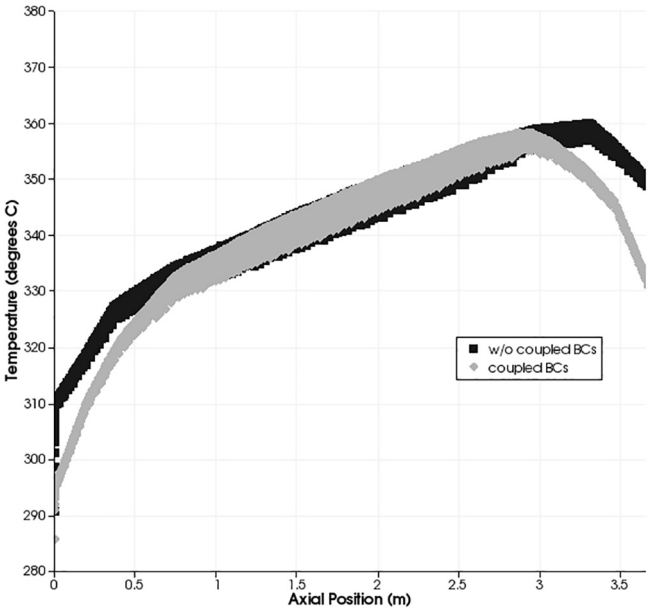

Fig. 12. Clad Inner Surface Temperature at One Year.

near the very bottom of the rod, the simulation without coupled boundary conditions results in an almost instantaneous jump in temperature from the inlet to the start of the rod's heated section. This behavior is not seen when feedback from the CTF-DeCART coupling is used. Below, Fig. 11 depicts the clad inner surface temperature at one day, and Fig. 12 shows the clad inner surface temperature at one year.

Similar to the clad outer surface temperature profiles, the clad inner surface temperature profiles in Fig. 11 generally follow the same shape. However, as noted with Fig. 9, the simulation without coupled boundary conditions shows a relatively larger change in slope near the bottom and top of the fuel rod. Comparing this change in slope with the power profile in Fig. 6, the slope of the relative power does not appear to change neat the top of the rod. Though other factors such as moderator temperature affect the temperature profile in the cladding, one would not expect the slope of the temperature profile to become less negative when the slope of the power profile remaining near constant. At the very least, it is known the slope of the axial power profile does not become less negative near the ends of the fuel rod. It should be noted that such is change is not seen when coupled boundary conditions are used in the BISON simulation.

Referring to Fig. 12, the BISON simulation calculates higher temperatures on the inner surface of the cladding near the top and bottom of the rod when not using coupled boundary conditions. At one year into the simulation, the jump from inlet temperature to the temperature at the first inner surface clad node in the heated section of the rod is even more drastic for the simulation without coupled boundary conditions than what was shown in Fig. 11. Clearly, the use of the CTF-DeCART coupling to provide

feedback for BISON simulations is having an effect on the temperature results inside the fuel rod. Those temperature results are then used to determine their effect on the redistribution of hydrogen in the cladding, as discussed in Section 6.2.

6.2. Hydrogen model results

Due to the computationally expensive nature of running a finite element code like BISON with time steps on the order of seconds, the size of the model was significantly reduced. For the CTF-DeCART, coupling the entire length of the fuel rod (360 pellets) is simulated; however, a five-pellet section of the fuel rod was chosen to be simulated in the hydrogen model. The five-pellet section was taken near the inlet of the full-length model. Subsequently, the coupled boundary conditions from this five-pellet section was extracted and used in the BISON and hydrogen model simulations. Fig. 13 below depicts the mesh that was used for the simulation in BISON. To analyze the effect of axial temperature gradients in the cladding, a two-dimensional model was built in BISON with dependence in the radial and axial directions. In addition, due to the symmetry of the fuel rod, only half of the rod is modeled in the radial direction.

Table 4 below shows the coupled power state conditions that were taken from the CTF-DeCART simulation. As noted earlier, the CTF-DeCART simulation was run for the full rod, but only a five-pellet section of power and temperature data was selected. Table 5 shows the coupled temperature boundary conditions from the CTF-DeCART simulation.

It should be noted that for the full-rod BISON simulation, a step function was used to impose the power profile. However, this was not done in the five-pellet simulation. DeCART axial cell sizes in this modeled were 20.32 cm; therefore, the five-pellet section was chosen at the border between two DeCART cells. On such a relatively small scale, imposing a step function does not significantly affect the temperature gradients in the cladding.

One of the challenges when attempting to model corrosion, and hydrogen diffusion and precipitation is limitations placed on time scaling. Generally, depletion calculations can remain accurate when using time steps on the order of days and months. Conversely, diffusion calculations require time steps on the order of seconds. When modeling a problem to run for four years, it is not practical to use time steps limited to ~200 s. Therefore, to overcome this challenge a uniform hydrogen concentration of 130 ppm was placed in the cladding as an initial condition. This specific initial concentration of hydrogen in the cladding was assumed to be high enough to allow the hydrogen precipitation process to take place. The hydrogen model was then started from the 3-year mark and simulated for one year, allowing the hydrogen to diffuse, precipitate, and also continue to ingress from corrosion of the waterside cladding surface. Fig. 14 below shows the cladding temperature as a function of radial position for two different axial elevations. The 'mid-pellet region' data was taken from the axial location along the cladding at the center of the third fuel pellet from the bottom (middle pellet). The 'inter-pellet gap' data was taken from the axial location along the cladding in between the second and third fuel pellet from the bottom. In addition, the data was extracted from the last time step at 4 years. Fig. 14 is used to observe how temperature affects the concentration of hydrogen in the cladding. Fig. 15 below shows the hydrogen in solid solution at two different elevations in the cladding. Fig. 16 highlights the precipitated hydrogen at the same two locations, and at the last time step. Fig. 17 also shows the precipitated hydrogen, but with the outermost node excluded.

Table 4
Axial Power Distribution for a Five-Pellet Section near the Bottom of a Full-Length Rod.

Time [days]	Relative Power	
	Bottom	Top
0	0.273	0.344
66	0.372	0.452
132	0.428	0.512
198	0.466	0.551
264	0.497	0.580
331	0.523	0.605
397	0.541	0.621
463	0.559	0.637
529	0.577	0.653
595	0.593	0.666
661	0.611	0.682
727	0.629	0.697
793	0.650	0.715
859	0.667	0.728
926	0.691	0.748
992	0.675	0.729
1058	0.663	0.716
2315	0.663	0.716

Table 5
Clad Outer Surface Temperature for a Five-Pellet Section near the Bottom of a Full-Length Rod.

Time [days]	Clad Outer Surface Temperature [°C]	
	Bottom	Top
0	295.3	296.9
66	297.8	299.7
132	299.2	301.2
198	300.0	302.0
264	300.5	302.6
331	301.0	303.0
397	301.2	303.2
463	301.5	303.5
529	301.8	303.7
595	302.0	303.8
661	302.2	304
727	302.4	304.2
793	302.7	304.4
859	302.8	304.5
926	303.1	304.7
992	302.7	304.2
1058	302.4	303.8
2315	302.4	303.8

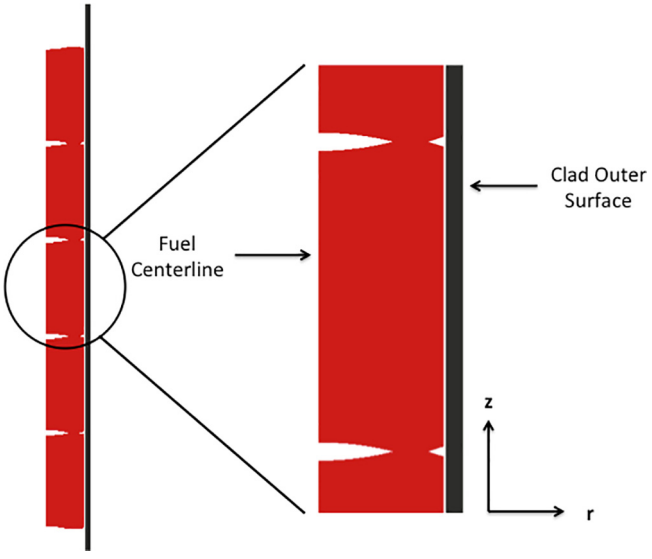

Fig. 13. Five-Pellet Mesh in BISON.

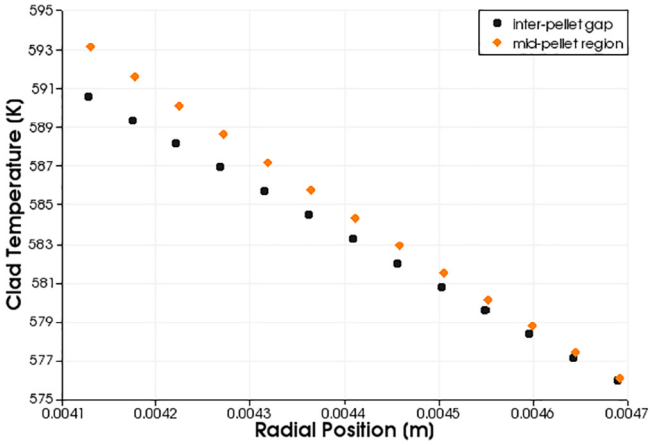

Fig. 14. Cladding temperature as a function of radial position after 4 years.

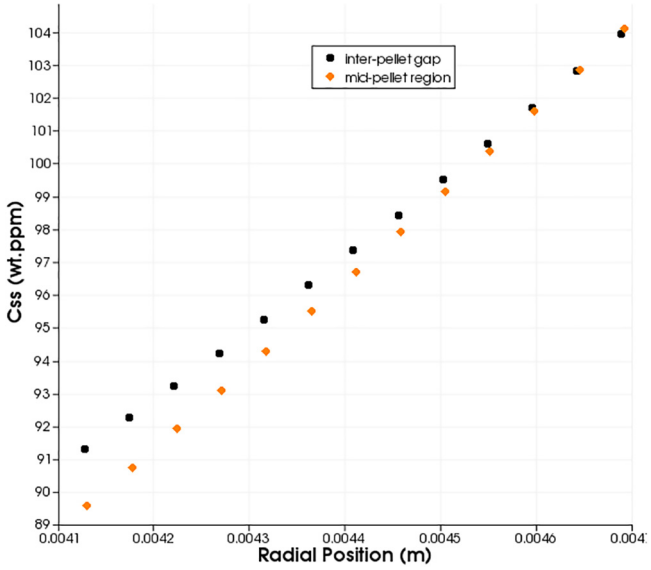

Fig. 15. Hydrogen in solid solution after 4 years.

Referring to Fig. 15, the hydrogen in solid solution at the inter-pellet gap on the inner surface of the cladding has a slightly higher concentration compared to the location at the mid-pellet region. Moving from the inner surface to the outer surface, the concentration of hydrogen in solid solution approaches the same value of about 104 wt ppm. This makes sense when comparing Figs. 14 and 15. The temperature on the inner surface of the cladding is higher at the mid-pellet region than at the inter-pellet gap. The decrease in temperature near the inter-pellet gap occurs because there is less fuel material at this location. Less fuel material equates to less fission, which ultimately leads to less energy deposition in the cladding with respect to the radial direction. As discussed in Section 1.2, the hydrogen diffuses in the opposite direction of positive temperature gradients. In other words, hydrogen will concentrate in areas of lower temperature. Though, it should be kept in mind the diffusion dues to a concentration often competes with diffusion due to a temperature gradient, attempting homogenize the concentration of hydrogen in the cladding. Considering these phenomenon, the colder temperatures in the inter-pellet gap region would, in fact, lead to a higher concentration of hydrogen in solid solution, which is exactly what is shown in Fig. 15. Furthermore, the change in temperature on the outside of the cladding at axial locations only 0.5 cm apart is trivial. Fig. 14 shows the temperatures on the outer surface of the cladding to be almost identical between the two regions. Therefore, it is expected that the hydrogen in solid solution will be identical as well.

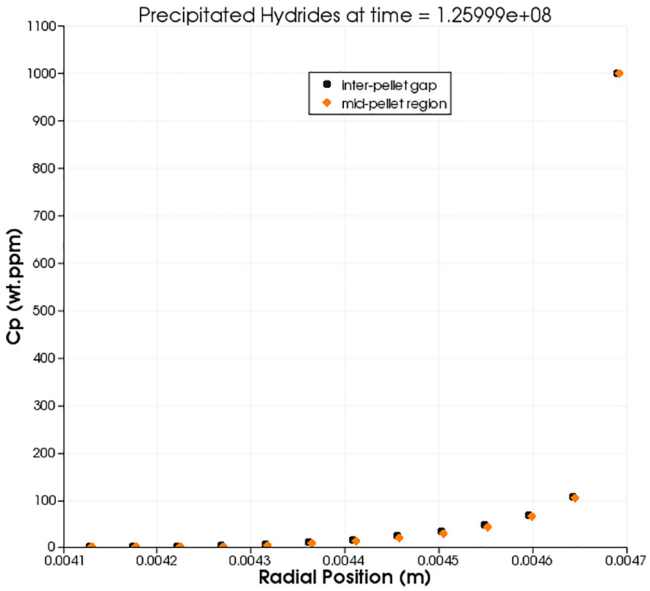

Fig. 16. Precipitated hydrides after 4 years.

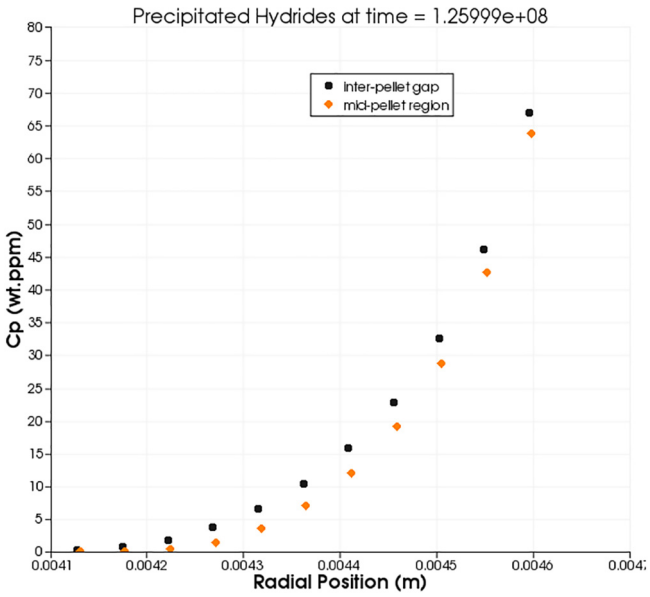

Fig. 17. Zoomed in view of precipitated hydrides after 4 years.

Referring Fig. 16, the formation of a hydride rim can be seen at both the inter-pellet gap and mid-pellet regions. Hydride rims have been observed and well documented through metallography experiments. A detailed explanation of the hydride rim formation and studies using the Hydrogen Model can be found in a separate publication titled, "Modeling and simulation of hydrogen behavior in Zircaloy-4 cladding" (Courty et al., 2014). To analyze the difference in hydride precipitation for axial regions, the outermost node (clad outer surface) was excluded and the remaining data points were plotted in Fig. 17. Note that the hydride concentration is higher at the inter-pellet gap than at the mid-pellet region. This makes sense because the inter-pellet gap has a higher overall concentration of hydrogen in solid solution than the mid-pellet region. With a higher concentration, the inter-pellet gap will reach the

TSSp quicker than the mid-pellet region. Thus, more hydrides precipitate in the inter-pellet gap region of the cladding. Though the absolute difference between the hydride concentrations is small, allowing the simulation to run for longer periods and the inclusion of a reactor shutdown in the boundary conditions would likely show greater dependence of the hydrogen diffusion on axial location.

7. Conclusions

Through the use of a multi-physics coupling between thermal-hydraulics, neutronics, and fuel performance codes, more realistic temperature calculations can be achieved, which allow for prediction of hydrogen diffusion and precipitation in the cladding of nuclear fuel rods. With this work, a tool has been developed which can model the degradation of nuclear fuel cladding, and ultimately target problem areas in the core. Moreover, future studies may lead to better prediction of fuel rod failures, and help to extend fuel rod lifetimes in the core. When comparing the cladding temperature calculations for BISON simulations with and without coupled boundary conditions, it was shown that the coupled boundary conditions provide better and more realistic results. The CTF-DeCART coupling allows for temperature and density data to be used as feedback for the cross section generation, and also for the power profiles to be used for feedback of the energy deposition into the coolant. Combining the use of the CTF-DeCART coupling with the Hydrogen Model implemented in BISON, it is now possible to observe the diffusion and precipitation of hydrogen in the cladding. The hydrogen distribution calculations have shown dependence in both the radial and axial directions.

At a specific axial height and azimuthal angle, the local hydride concentration might be very high forming a weak point in the cladding. Therefore, a three-dimensional (3D model) BISON is needed to be able to completely quantify this local effect. A 2D (r-z) BISON model might average out this local effect and underestimate its impact on the cladding.

Currently, ongoing work in this project aims to select fuel rods located in areas of higher risk for corrosion (i.e. assembly periphery, adjacent to guide tubes, presence of strong power gradients, etc.) and test the coupling and hydrogen model on these rods. The rods will be modeled in three dimensions with respect to the axial, radial and azimuthal directions. The hope is that in the future this hydrogen model/coupling tool will be able to predict problem areas in the core for cladding degradation due to the presence of precipitated hydrides.

Acknowledgements

The work reported in this paper is supported by the US DOE NEUP Project 11-1722 entitled “Anisotropic azimuthal power and temperature distribution on fuel rod: impact on hydride distribution”.

References

Avramova, M., 2016. CTF - A Modernized Thermal-Hydraulic Subchannel Code for Reactor Core and Vessel Analyses. North Carolina State University.
Colas, K., 2012. Fundamental experiments on hydride reorientation in Zircaloy. PhD in Nuclear Engineering. Pennsylvania State University.
Courty, O., 2013. Hydrogen distribution in zircaloy under a temperature gradient: modeling, simulation, and experiment. MS in Nuclear Engineering. Pennsylvania State University.
Courty, O., Motta, A., Hales, J., 2014. Modeling and simulation of hydrogen behavior in Zircaloy-4 fuel cladding. J. Nucl. Mater. 452, 311–320.
Derek Gaston, J., 2012. MOOSE Workshop. Idaho National Laboratory: MIT.
Geelhood, K., Luscher, W., Beyer, C., 2011. FRAPCON-3.4: Integral Assessment. Pacific Northwest National Laboratory.
Hamilton, S. et al., 2012. Integrated radiation transport and nuclear fuel performance for assembly-level simulations. In: Proceedings of PHYSOR 2012 Conference, 2012: Knoxville, TN.
Hursin, M., Downar, T., Kochunas, B., 2008. PWR Control Rod Ejection Analysis with the Method of Characteristic Code DeCART. In: Proceedings of PHYSOR 2008 Conference: Interlaken, Switzerland.
INSAG, 1996. Defense in Depth in Nuclear Safety. IAEA publications.
Kammenzind, B. et al., 1996. Hydrogen pickup and redistribution in alpha-annealed Zircaloy-4. In: Zirconium in the Nuclear Industry: 11th International Symposium. ASTM STP 1295: p. 338-370.
Kearns, J., 1967. Terminal solubility and partitioning of hydrogen in the alpha phase of zirconium, Zircaloy-2 and Zircaloy-4. J. Nucl. Mater. 22 (3), 292–303.
Kearns, J., 1972. Diffusion coefficient of hydrogen in alpha zirconium, Zircaloy-2 and Zircaloy-4. J. Nucl. Mater. 43, 330–338.
Kochunas, B., Hursin, M., Downar, T., 2009. DeCART-v2.05 Theory Manual. University of Michigan.
Laboratory, K.I.L.A.N., Paraview, 2013: http://www.paraview.org.
McMinn, A., Darby, E., Schofield, J., 2000. The Terminal Solid Solubility of Hydrogen in Zirconium Alloys. In: Zirconium in the Nuclear Industry: Twelfth International Symposium, 2000. ASTM STP 1354: p. 173–195.
Sawatzky, A., 1960. Hydrogen in zircaloy-2: its distribution and heat of transport. J. Nucl. Mater. 4, 321–328.
Sawatzky, A., Ells, C., 2000. Understanding Hydrogen in Zirconium. In: Zirconium in the nuclear industry: Twelfth international symposium ASTM STP 1354, West Conshohocken, Pennsylvania, pp 32–48.
Studsvik, 2009. SIMULATE-3: Advanced Three-Dimensional Two-Group Reactor Analysis Code.
Wagner, J., DeHart, M., Parks, C., 2003. Recommendations for Addressing Axial Burnup in PWR Burnup Credit Analyses. Oak Ridge National Laboratory.
Williamson, R., Novascone, J., Spencer, B., 2012a. BISON Workshop. INL Laboratory. Edition.
Williamson, R. et al., 2012b. Multidimensional multiphysics simulation of nuclear fuel behavior. J. Nucl. Mater. 423 (1–3), 149–163.
Xu, J., Shi, S., 2004. Investigation of mechanical properties of epsilon-zirconium hydride using micro- and nano-indentation techniques. J. Nucl. Mater. 327, 165–170.